AIChE Letter. Advances in Materials: Inorganic Materials: Synthesis and Processing

In Situ Metal Doping During Modified Anodization Synthesis of Nb_2O_5 with Enhanced Photoelectrochemical Water Splitting

Chenyan Hu and Wey Yang Teoh
Clean Energy and Nanotechnology (CLEAN) Laboratory, School of Energy and Environment, City University of Hong Kong, Kowloon, Hong Kong S.A.R.

Shulin Ji and Changhui Ye
Anhui Key Laboratory of Nanomaterials and Technology and Key Laboratory of Materials Physics, Institute of Solid State Physics, Chinese Academy of Sciences, P.R. China

Akihide Iwase
Dept. of Applied Chemistry, Tokyo University of Science, Tokyo, Japan

DOI 10.1002/aic.15048
Published online October 1, 2015 in Wiley Online Library (wileyonlinelibrary.com)

Significance

A new technique of in situ doping of alkali metal (Li^+, Na^+, K^+, Rb^+, and Cs^+) in Nb_2O_5 was showcased by the modified anodization of Nb foils at high frequency, negative-to-positive pulsed voltage. At the optimized dopant concentration and synthesis condition, the doped-Nb_2O_5 shows twofold enhancement in photoelectrochemical water splitting efficiencies compared with the undoped Nb_2O_5 electrode, as a result of improved charge carrier density and enhanced surface charge transfer. *AIChE J*, 62: 352–358, 2016
Keywords: water splitting, hydrogen, photoelectrode, pulsed anodization, doping

The rapid implementation of hydrogen economy as a potential solution to the Energy crisis is urgently seeking the development of new materials for sustainable H_2 production. In particular, the investigation of oxide semiconductors for the applications in solar photoelectrochemical (PEC) water splitting is arguably one of the most active areas of research undertaken in the recent decade. Challenges stem from the long-standing requirements for a single material that possesses efficient solar absorption, appropriate band edge potentials for H_2 and O_2 evolution, high quantum efficiency, and long-term photostability.[1–4] Despite being far-fetching, significant progress in the discovery of new materials and modifications has been made to address each of the requirements in an (inevitable) independent fashion.

In terms of materials modification, the doping with foreign cations or anions is a classic but effective strategy.[5,6] For example, the N^{2-} doping in TiO_2 and other wide bandgap semiconductors extends the photoresponse to the visible light by creating new sub-bandgap energy levels,[7–9] while cationic dopants, such as Mo^{6+} and W^{6+}, Ti^{4+}, and Sn^{4+}, could act as electron donors to establish more sufficient conductivities in $BiVO_4$[10] and α-Fe_2O_3,[11,12] further resulting in enhanced charge transport. Unlike the well-studied wide bandgap oxides, such as TiO_2, ZnO, and WO_3, Nb_2O_5 is not known to exhibit high PEC water splitting efficiencies despite possessing suitable conduction and valence band edge potentials.[13,14] As such, there is potential to significantly improve its efficiencies through the strategies of doping and nanostructuring. Here, we introduce a new protocol based on modified pulsed anodization where alkali metal cations ($M = Li^+$, Na^+, K^+, Rb^+, and Cs^+, representing increasing ionic radii in the same order) can be *in situ* doped into Nb_2O_5 to improve its efficiency in PEC water splitting. To the best of our knowledge, the work is the first to synthesize cationic-doped Nb_2O_5

Additional Supporting Information may be found in the online version of this article.

Correspondence concerning this article should be addressed to W. Y. Teoh at wyteoh@cityu.edu.hk.

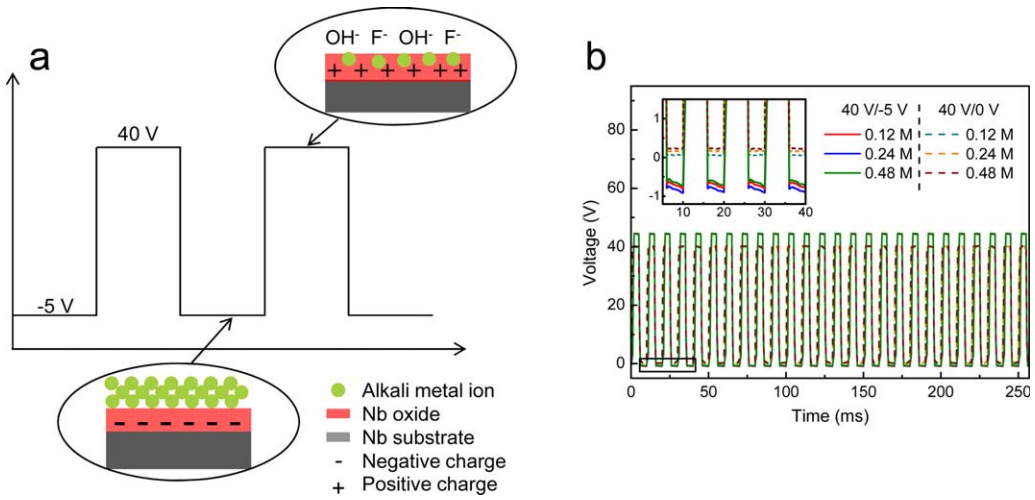

Figure 1. (a) Scheme of the modified pulsed anodization process. (b) Transient voltage pattern during the pulsed anodization of Nb films at voltage levels of (40 V/−5 V) and (40 V/0 V) in CsF containing electrolytes. Inset is the enlargement of the zero or negative pulses.

[Color figure can be viewed in the online issue, which is available at wileyonlinelibrary.com.]

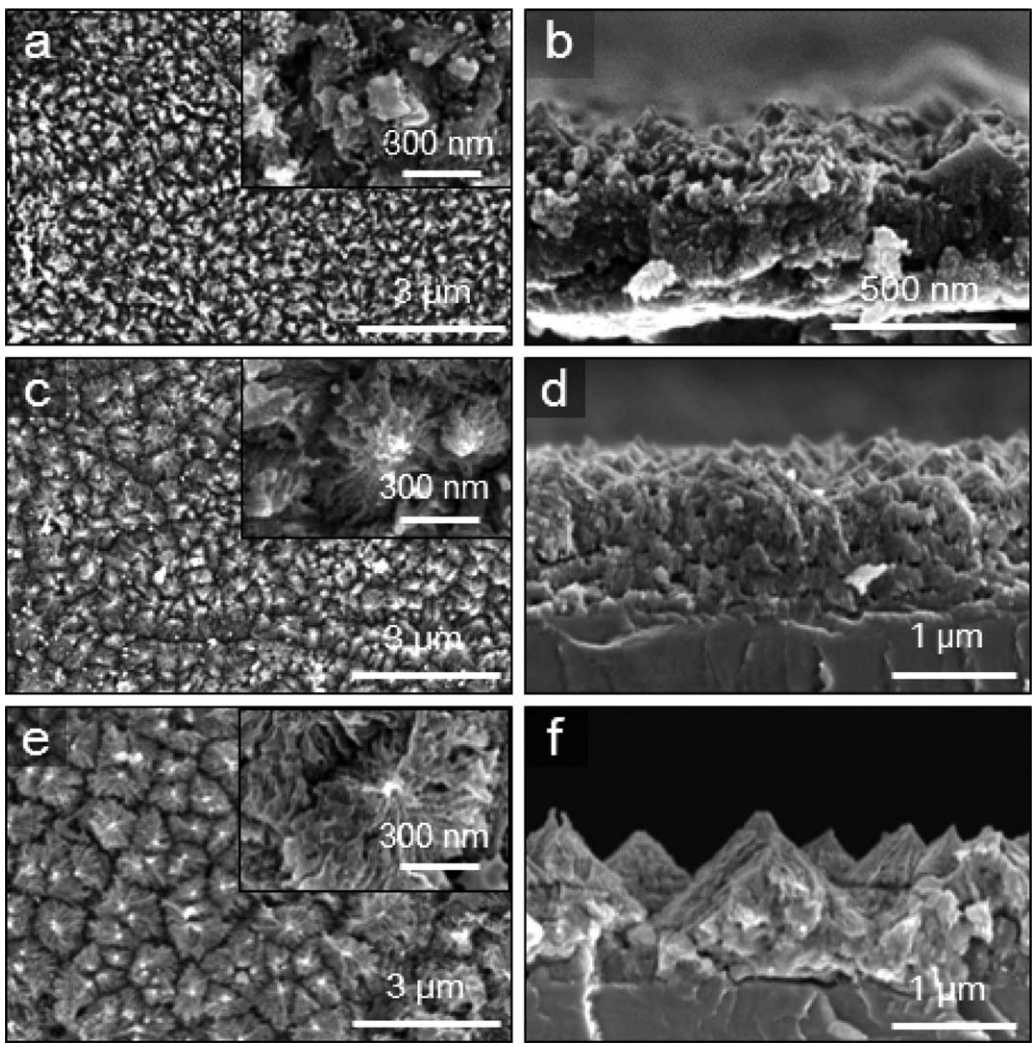

Figure 2. Top view images of $Cs_{(x)}$-Nb_2O_5 (40 V/−5 V) films prepared by pulsed anodization in 1.0 M H_2SO_4 aqueous electrolytes containing (a) 0.12 M, (c) 0.24 M, and (e) 0.48 M CsF for 40 min. Also shown are their corresponding cross-sectional images (b), (d), and (f). The magnified images of (a), (c), and (e) are shown in their insets.

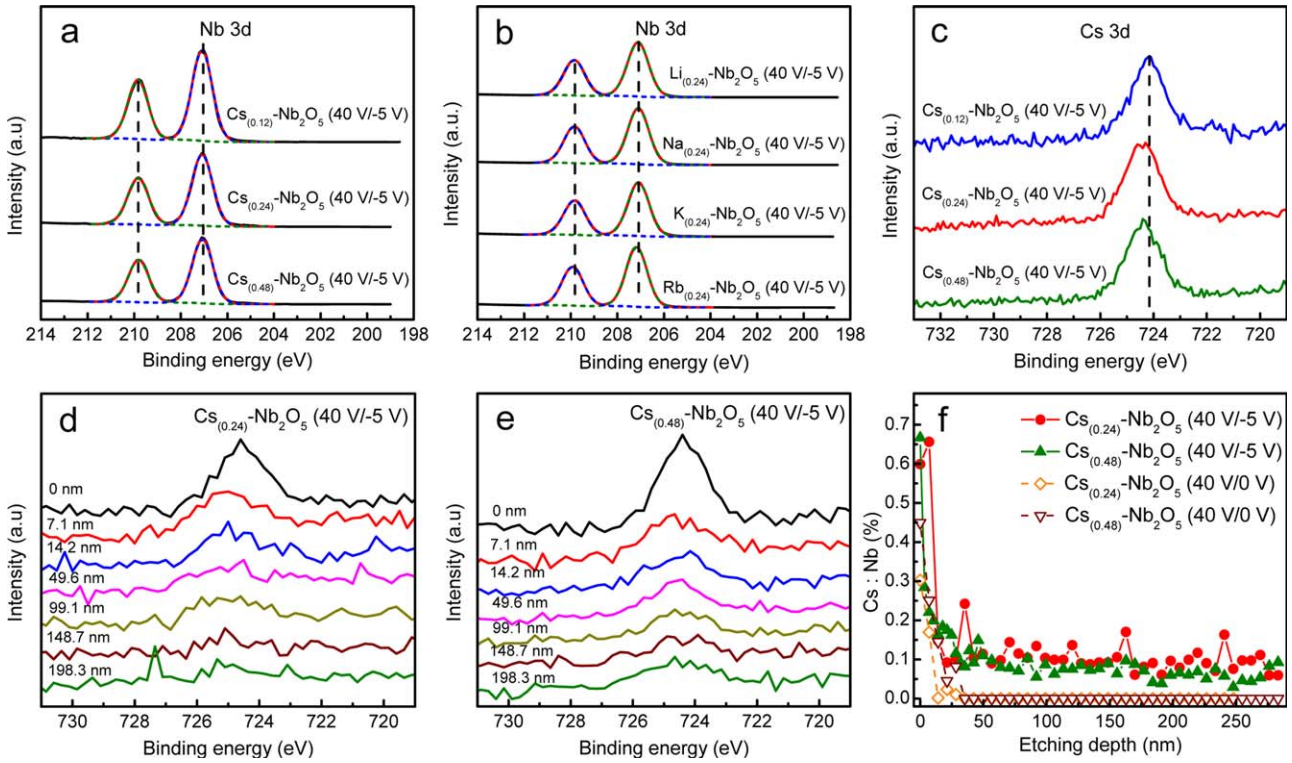

Figure 3. Surface Nb 3d XPS spectra of (a) $Cs_{(x)}$-Nb_2O_5 (40 V/−5 V) films anodized in 0.12, 0.24, and 0.48 M CsF electrolytes and (b) $M_{(0.24)}$-Nb_2O_5 (40 V/−5 V) films prepared in 0.24 M LiF, NaF, KF, and RbF electrolytes, respectively. (c) Cs 3d XPS spectra of $Cs_{(x)}$-Nb_2O_5 (40 V/−5 V) surfaces prepared at different CsF concentrations. Cs 3d XPS spectra of (d) $Cs_{(0.24)}$-Nb_2O_5 (40 V/−5 V) and (e) $Cs_{(0.48)}$-Nb_2O_5 (40 V/−5 V) films at different sputtering depths. (f) Depth profiles showing the atomic ratios of Cs and Nb in $Cs_{(0.24)}$-Nb_2O_5 (40 V/−5 V), $Cs_{(0.48)}$-Nb_2O_5 (40 V/−5 V), and the corresponding Nb_2O_5 films anodized at pulsed voltage of (40 V/0 V).

[Color figure can be viewed in the online issue, which is available at wileyonlinelibrary.com.]

electrodes using such *in situ* anodization method, which in principle can be extended to a wide variety of combinations of metal cations and anodized metal oxide films.

In the modified pulsed anodization, a highly positive voltage is alternated with a slightly negative voltage in a square wave pattern (Figure 1a). While the purpose of the positive voltage is for the anodization of the Nb foil (similar to the conventional anodization), the negative voltage functions to electrostatically attract the alkali metal cations to the surface of the foil. A rapid rise to the positive voltage oxidizes the Nb foil in the presence of the alkali metal cations dopant. The positive voltage of the pulsed anodization was set at 40 V for a total duration of 40 min, a condition which we earlier optimized using the steady voltage anodization (Supporting Information Figure S1). The negative voltage was set nominally at −5 V (See the experimental section in Supplementary Information). As shown in the inset of Figure 1b, only an actual voltage of approximately −0.7 V could be reached due to the internal large resistance from the oxide layer formation in the preceding cycles.[15] In our case, applying a more negative voltage would compromise on the maximum reachable positive voltage, that is, <40 V. For convenience, the optimized nominal positive and negative voltages are represented by the connotation (40 V/−5 V). Variation of the alkali metal dopants will be expressed by their elements and concentrations in the electrolytes. For example, the sample anodized at (40 V/−5 V) in electrolyte containing 0.12 M CsF will be denoted $Cs_{(0.12)}$-Nb_2O_5 (40 V/−5 V). In all cases the frequency of the pulsed anodization is 100 Hz.

The field emission-scanning electron microscopy images of $Cs_{(x)}$-Nb_2O_5 (40 V/−5 V) films synthesized in the presence of 0.12, 0.24, and 0.48 M CsF electrolytes are displayed in Figure 2. Unlike the Nb_2O_5 nanorods obtained at constant 40 V for the same duration (Supporting Information Figures S1a, b), these Nb_2O_5 films showed the hierarchical conical structures formed from the bundling of nanorods (insets of Figures 2a, c, and e). Similar nanocones of Nb_2O_5 could also be obtained but with extended anodization duration (>2 h) at constant 40 V (Supporting Information Figures S1d–f). With increasing the CsF concentration in electrolyte, the cones augmented in size, indicating the enhanced cone evolution by larger electrolyte conductivity.[16] As such, the thickness of the oxide film was also increased from 0.44, 1.08 to 1.17 μm when the CsF concentration was increased from 0.12, 0.24 to 0.48 M, respectively (Figures 2b, d, and f). Similar hierarchical conical structures were obtained from other alkali metal containing electrolytes, shown here for $Li_{(0.24)}$-, $Na_{(0.24)}$-, $K_{(0.24)}$-, and $Rb_{(0.24)}$-Nb_2O_5 (40 V/−5 V) with respective thickness of 1.02, 1.24, 1.38, and 1.77 μm (Supporting Information Figure S2).

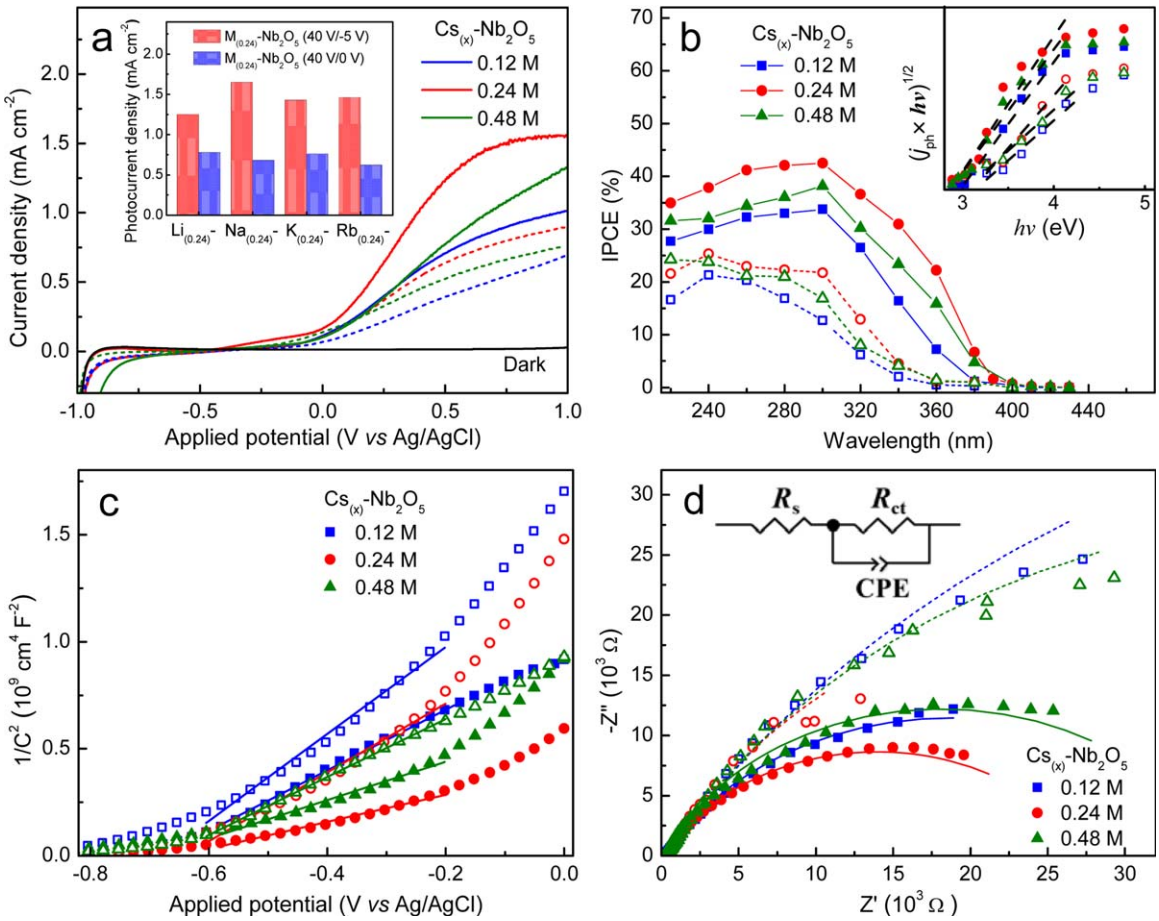

Figure 4. (a) Photocurrent response of $Cs_{(x)}$-Nb_2O_5 (40 V/−5 V) (solid line) and $Cs_{(x)}$-Nb_2O_5 (40 V/o V) (dash line) electrodes prepared at different CsF concentrations in electrolytes. Inset is the photocurrent density of different alkali metal ions doped $M_{(0.24)}$-Nb_2O_5 (40 V/−5 V) and undoped $M_{(0.24)}$-Nb_2O_5 (40 V/o V) electrodes at +1.0 V vs. Ag/AgCl. (b) IPCE spectra and the Tauc plot as inset, (c) Mott-Schottky plot, and (d) Nyquist plot of the $Cs_{(x)}$-Nb_2O_5 (40 V/−5 V) (solid symbol) and $Cs_{(x)}$-Nb_2O_5 (40 V/o V) (open symbol) electrodes with the equivalent circuit to model the electrochemical impedance spectra as inset.

[Color figure can be viewed in the online issue, which is available at wileyonlinelibrary.com.]

Upon annealing at 500°C for 3 h in N_2 atmosphere, the $M_{(x)}$-Nb_2O_5 films can be characterized by the orthorhombic Nb_2O_5 structure (ICDD 27-1003) (Supporting Information Figure S3), inferring unmodified lattice parameters compared with the pristine control film, most likely due to the limited dopant concentrations (<0.5% based on the sensitivity of X-ray diffraction, (XRD)). For more local information of the Nb_2O_5 and the dopants, the X-ray photoelectron spectroscopy (XPS) was used. As shown in Figures 3a, b, the pulsed anodized samples consist of the Nb $3d_{5/2}$ and $3d_{3/2}$ binding energy peaks centered at 207.1 and 209.9 eV, belonging to the Nb^{5+} species in Nb_2O_5,[17,18] corroborating the XRD analyses that only the Nb_2O_5 phase was formed. Surface analyses of the Cs 3d of $Cs_{(0.12)}$-, $Cs_{(0.24)}$-, and $Cs_{(0.48)}$-Nb_2O_5 (40 V/−5 V) show peaks centered at 724.2 eV belonging to the Cs^+ of CsOH (Figure 3c).[19] These are strongly adsorbed surface Cs^+ residues from the electrolyte. As the surface is sputtered to reveal the subsurface local information at different depths, the Cs 3d binding energy peaks are shifted to 725.0 eV, revealing the presence of Cs_2O dopant species (Figures 3d, e).[20] The distribution of the Cs^+ dopant ions is further plotted as a function of the film depths (Figure 3f), where a steep surface concentration of Cs can be observed up to the depth of ~40 nm before reaching the bulk dopant concentration of ~0.1% Cs with respect to Nb. Given the large ionic radii of Cs^+ (1.69 Å) relative to Nb^{5+} (0.7 Å), the dopant is more likely to be substitutionally doped than interstitially doped. As a reference, the dopant depth profiles of $Cs_{(x)}$-Nb_2O_5 (40 V/0 V), despite having similar hierarchical conical morphologies (Supporting Information Figure S4), do not show any amount of Cs^+ present in the bulk beyond the residues accumulated on the surfaces (Figure 3f). Compared with the previous reports on pulsed anodization,[21,22] the high frequency (100 Hz) used in this work is one of the contributing factors toward successful cationic doping. Only in this way, the adsorbed alkali metal ions could be retained in the Nb_2O_5 films instead of being removed by the etching-anodization.

The cationic-doped $M_{(x)}$-Nb_2O_5 (40 V/−5 V) electrodes were assessed for PEC water splitting. Figure 4a shows the current-potential curves of the $Cs_{(x)}$-Nb_2O_5 (40 V/−5 V)

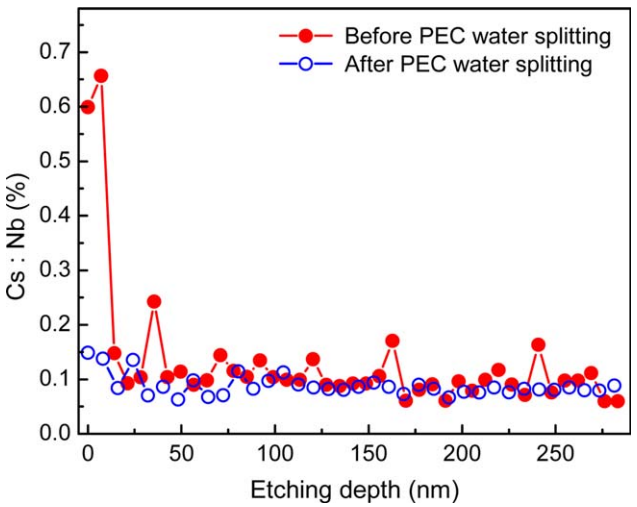

Figure 5. Depth profiles showing the atomic ratio of Cs and Nb in $Cs_{(0.24)}$-Nb_2O_5 (40 V/−5 V) electrode before and after the PEC water splitting.

[Color figure can be viewed in the online issue, which is available at wileyonlinelibrary.com.]

electrodes. For comparison, the PEC properties of the undoped $Cs_{(x)}$-Nb_2O_5 (40 V/0 V) are also given. All the electrodes showed negligible dark currents in the scanned potential range. Under photoexcitation, the undoped $Cs_{(0.12)}$-Nb_2O_5 (40 V/0 V) generated comparable photocurrent as that prepared under constant voltage (Supporting Information Figure S1). Doping of Cs^+ enhanced the photocurrent by almost twofold, where $Cs_{(0.24)}$-Nb_2O_5 (40 V/−5 V) generated the highest photocurrent of 1.52 mA cm^{-2} at +1.0 V vs. Ag/AgCl compared with 0.86 mA cm^{-2} for $Cs_{(0.24)}$-Nb_2O_5 (40 V/0 V). Importantly, the bulk Cs^+ dopant content was retained after PEC water splitting while the surface adsorbed CsOH was removed (Figure 5). The effect of other cationic dopants is shown in the inset of Figure 4a, again showing photocurrent enhancement in all doped samples ($M_{(0.24)}$-Nb_2O_5 (40 V/−5 V)) relative to the pristine references ($M_{(0.24)}$-Nb_2O_5 (40 V/0 V)). As noted, the Na^+-doped Nb_2O_5 yielded the highest photocurrent of 1.65 mA cm^{-2} at +1.0 V vs. Ag/AgCl. Figure 4b shows the incident photon-to-current conversion efficiencies (IPCE) of the Cs^+-doped and undoped Nb_2O_5 electrodes. The highest IPCE of 42% was measured at 300 nm for the optimum $Cs_{(0.24)}$-Nb_2O_5 (40 V/−5 V), compared with 22% for the undoped sample. The equivalent IPCE for the Na^+-doped Nb_2O_5 electrode reached 50% (Supporting Information Figure S5a). As shown in the insets of Figure 4b (and Supporting Information Figure S5b), the bandgaps of the pristine and doped Nb_2O_5 were estimated by extending the linear portion of $(j_{ph} \times h\nu)^{1/2}$ vs. $h\nu$ to the abscissa, in a PEC equivalence of the Tauc plot.[23] Given the low dopant concentrations, the doped samples are not expected to exhibit significant modification in the band structure. The intrinsic bandgap of the undoped Nb_2O_5 was 3.1–3.2 eV, and on doping with alkali metal cations, slight decrease in the bandgap values to 2.9–3.0 eV was measured (Supporting Information Table S1). This is consistent with alkali metal (Na^+, K^+, Rb^+, Cs^+)-doped Ta_3N_5 photoelectrodes.[24]

To gain insights on the electronic properties of the doped-Nb_2O_5, the Mott-Schottky (M-S) plot was used and is shown in Figure 4c for $Cs_{(x)}$-Nb_2O_5 electrodes. All samples, both doped and undoped, are characterized by the positive slopes in the M-S plots as typical of *n*-type semiconductors. From the slope in the quasilinear region close to the flatband potential (E_{fb}), the charge carrier densities (N_A) of $Cs_{(0.12)}$-, $Cs_{(0.24)}$-, and $Cs_{(0.48)}$-Nb_2O_5 (40 V/−5 V) electrodes were estimated to be 7.9, 17.8, and 12.4 × 10^{18} cm^{-3}, respectively. By comparison, the charge carrier densities of the respective non-negative pulsed electrodes were only 5.5, 7.0, and 8.3 × 10^{18} cm^{-3}. Likewise, substantial increase in charge carrier density was recorded for Li^+, Na^+, K^+, and Rb^+-doped Nb_2O_5 electrodes (Supporting Information Figure S6, Table S1). In principle, doping improves the bulk charge transport properties as reflected by the enhanced charge carrier density,[6,12,25] and gives rise to the enhanced quantum efficiencies. The flatband potentials (E_{fb}) of these Nb_2O_5 electrodes (∼ −0.67 V vs. Ag/AgCl) were only marginally affected by the presence of alkali metal cationic dopants, again pointing to the minimal of shifting of the intrinsic Nb_2O_5 band potentials given the low amount of dopants.

To characterize the interfacial charge transfer of the electrodes, we performed the electrochemical impedance measurement as depicted by the Nyquist plots (Figure 4d and Supporting Information Figure S7). In each case, the depressed arc can be adequately described with an equivalent circuit, consisting of the electrolyte resistance (R_s), charge transfer resistance at the photoelectrode-electrolyte interface (R_{ct}), and a constant phase element (inset of Figure 4d).[26] The fitted parameters are tabulated in Supporting Information Table S1. The R_{ct} of the doped samples were significantly lowered compared with the undoped samples, inferring favorable interfacial charge transfer at the doped electrode surface for the oxygen evolution reaction (OER). This, and the enhanced charge carrier densities in the doped-Nb_2O_5 electrodes are the main reasons for their high efficiencies.

To further improve the performance of the optimum Cs^+-doped Nb_2O_5 electrode, we deposited cobalt-phosphate (Co-Pi) OER cocatalyst on the electrode surface by photodeposition.

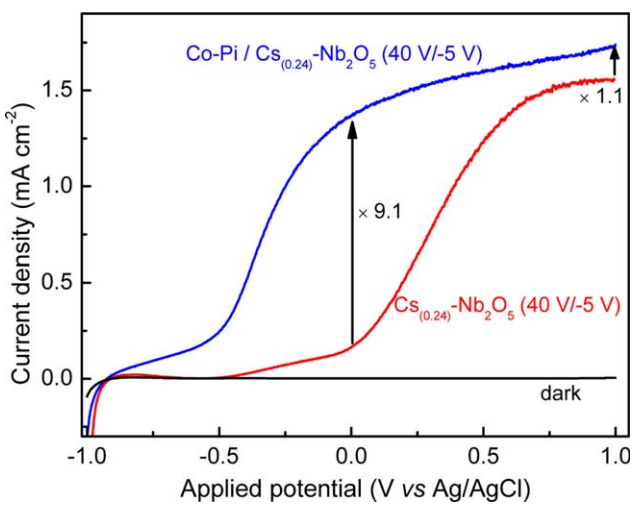

Figure 6. Photocurrent response of bare and Co-Pi deposited Cs_x-Nb_2O_5 (40 V/−5V) electrodes.

[Color figure can be viewed in the online issue, which is available at wileyonlinelibrary.com.]

As shown in Figure 6, the presence of Co-Pi significantly enhanced the photocurrent response especially at low potentials where the photocurrent was enhanced by more than ninefold to 1.37 mA cm^{-2} at 0 V vs. Ag/AgCl. In other words, the surface extraction of minority carriers is a major limiting step under low applied potentials. With the deposition of Co-Pi, the overpotential of OER was lowered by ~0.3 V. In contrast, the photocurrent density was only mildly improved ~10% at +1.0 V vs. Ag/AgCl as at such high potential the surface charge transfer is no longer a limiting step. Our attempt to passivate any surface recombination centers by introducing Al_2O_3, TiO_2, and SiO_2 barrier layers did not result in any significant improvements in photocurrent densities (Supporting Information Table S2), implying that surface charge recombination is not a major limitation for our photoelectrodes.[27]

In summary, a facile protocol for the *in situ* doping of foreign cations during the anodization synthesis was introduced. The concept was demonstrated with the synthesis of alkali metal (Li^+, Na^+, K^+, Rb^+, and Cs^+)-doped Nb_2O_5 electrodes. The doped-Nb_2O_5 electrodes showed improved efficiencies in PEC water splitting, almost doubled that of the undoped electrodes. This was traced to the enhanced charge carrier density and favorable charge transfer of the doped electrode. Surface deposition of Co-Pi cocatalyst further improved the PEC activities of the alkali metal doped Nb_2O_5 electrodes through the lowering of OER overpotential. In principle, the modified anodization technique can be conveniently extended to the synthesis of other new materials with homogeneously doped structures.

Acknowledgments

The work is financially supported by the Research Grant Council of Hong Kong through the General Research Fund (Project 103311).

Literature Cited

1. Teoh W, Scott J, Amal R. Progress in heterogeneous photocatalysis: from classical radical chemistry to engineering nanomaterials and solar reactors. *J Phys Chem Lett*. 2012;3:629–639.
2. Liu J, Hisatomi T, Ma G, Iwanaga A, Minegishi T, Moriya Y, Katayama M, Kubota J, Domen K. Improving the photoelectrochemical activity of $La_5Ti_2CuS_5O_7$ for hydrogen evolution by particle transfer and doping. *Energy Environ Sci*. 2014;7:2239–2242.
3. Yang H, Kershaw S, Wang Y, Gong X, Kalytchuk S, Rogach A, Teoh W. Shuttling photoelectrochemical electron transport in tricomponent CdS/rGO/TiO_2 nanocomposites. *J Phys Chem C*. 2013;117:20406–20414.
4. Kho Y, Teoh W, Iwase A, Mädler L, Kudo A, Amal R. Flame preparation of visible-light-responsive $BiVO_4$ oxygen evolution photocatalysts with subsequent activation via aqueous route. *ACS Appl Mater Interfaces*. 2011;3:1997–2004.
5. Asahi R, Morikawa T, Ohwaki T, Aoki K, Taga Y. Visible-light photocatalysis in nitrogen-doped titanium oxides. *Science*. 2001;293:269–271.
6. Kleiman-Shwarsctein A, Huda M, Walsh A, Yan Y, Stucky G, Hu Y, Jassim M, McFarland E. Electrodeposited aluminum-doped α-Fe_2O_3 photoelectrodes: experiment and theory. *Chem Mater*. 2010;22:510–517.
7. Nah Y, Paramasivam I, Hahn R, Shrestha N, Schmuki P. Nitrogen doping of nanoporous WO_3 layers by NH_3 treatment for increased visible light photoresponse. *Nanotechnology*. 2010;21:105704.
8. Qiu Y, Yan K, Deng H, Yang S. Secondary branching and nitrogen doping of ZnO nanotetrapods: building a highly active network for photoelectrochemical water splitting. *Nano Lett*. 2011;12:407–413.
9. Yang X, Wolcott A, Wang G, Sobo A, Fitzmorris R, Qian F, Zhang J, Li Y. Nitrogen-doped ZnO nanowire arrays for photoelectrochemical water splitting. *Nano Lett*. 2009;9:2331–2336.
10. Park H, Kweon K, Ye H, Paek E, Hwang G, Bard A. Factors in the metal doping of $BiVO_4$ for improved photoelectrocatalytic activity as studied by scanning electrochemical microscopy and first-principles density-functional calculation. *J Phys Chem C*. 2011;115:17870–17879.
11. Hahn N, Mullins C. Photoelectrochemical performance of nanostructured Ti- and Sn-doped α-Fe_2O_3 photoanodes. *Chem Mater*. 2010;22:6474–6482.
12. Ling Y, Wang G, Wheeler D, Zhang J, Li Y. Sn-doped hematite nanostructures for photoelectrochemical water splitting. *Nano Lett*. 2011;11:2119–2125.
13. Li L, Deng J, Yu R, Chen J, Wang Z, Xing X. Niobium pentoxide hollow nanospheres with enhanced visible light photocatalytic activity. *J Mater Chem A*. 2013;1:11894–11900.
14. de Filho D, Franco D, Filho P, Alves O. Niobia films: surface morphology, surface analysis, photoelectrochemical properties and crystallization process. *J Mater Sci*. 1998;33:2607–2616.
15. Lee W, Scholz R, Gösele U. A continuous process for structurally well-defined Al_2O_3 nanotubes based on pulse anodization of aluminum. *Nano Lett*. 2008;8:2155–2160.
16. Yoo J, Park J, Cha G, Choi J. Micro-length anodic porous niobium oxide for lithium-ion thin film battery applications. *Thin Solid Films*. 2013;531:583–587.
17. Yao D, Rani R, O'Mullane A, Kalantar-zadeh K, Ou J. High performance electrochromic devices based on anodized nanoporous Nb_2O_5. *J Phys Chem C*. 2013;118:476–481.
18. Allam N, Alamgir F, El-Sayed M. Enhanced photoassisted water electrolysis using vertically oriented anodically fabricated Ti-Nb-Zr-O mixed oxide nanotube arrays. *ACS Nano*. 2010;4:5819–5826.
19. Moulder J, Stickle W, Sobol P, Bomben K. *Handbook of X-Ray Photoelectron Spectroscopy*, Minnesota, USA: Physical Electronics, Inc, 1995.
20. Ebbinghaus G, Simon A. Electronics structures of Rb, Cs and some of their metallic oxides studied by photoelectron spectroscopy. *Chem Phys*. 1979;43:117–133.
21. Lee W, Schwirn K, Steinhart M, Pippel E, Scholz R, Gosele U. Structural engineering of nanoporous anodic aluminium oxide by pulse anodization of aluminium. *Nat Nanotechnol*. 2008;3:234–239.
22. Liu Y, Wang D, Cao L, Chen S. Structural engineering of highly ordered TiO_2 nanotube array by periodic anodization of titanium. *Electrochem Commun*. 2012;23:68–71.
23. Beranek R, Tsuchiya H, Sugishima T, Macak J, Taveira L, Fujimoto S, Kisch H, Schmuki P. Enhancement and

limits of the photoelectrochemical response from anodic TiO_2 nanotubes. *Appl Phys Lett*. 2005;87:243114.
24. Kado Y, Lee C-Y, Lee K, Muller J, Moll M, Spiecker E, Schmuki P. Enhanced water splitting activity of M-doped Ta_3N_5 (M = Na, K, Rb, Cs). *Chem Commun*. 2012;48:8685–8687.
25. Parmar K, Kang H, Bist A, Dua P, Jang J, Lee J. Photocatalytic and photoelectrochemical water oxidation over metal-doped monoclinic $BiVO_4$ Photoanodes. *ChemSusChem*. 2012;5:1926–1934.
26. Jo W, Jang J-W, Kong K-j, Kang H, Kim J, Jun H, Parmar K, Lee J. Phosphate doping into monoclinic $BiVO_4$ for enhanced photoelectrochemical water oxidation activity. *Angew Chem Int Ed*. 2012;51:3147–3151.
27. Hu C, Chu K, Zhao Y, Teoh W. Efficient photoelectrochemical water splitting over anodized p-type NiO porous films. *ACS Appl Mater Interfaces*. 2014;6:18558–18568.

Manuscript received May 29, 2015, and revision received Aug. 17, 2015.